Clays and Clay Minerals (2025), **73**, e4, 1–13
doi:10.1017/cmn.2024.35

Original Paper

Mineralogy and crystal-chemistry of trioctahedral smectites from Turkey

Adrián Lorenzo[1], Emilia García-Romero[2,3], Mefail Yeniyol[4] and Mercedes Suárez[1]

[1]Department of Geology, University of Salamanca, 37008 Salamanca, Spain; [2]Department of Mineralogy and Petrology, Complutense University of Madrid, 28040 Madrid, Spain; [3]Geosciences Institute (IGEO)-Spanish Research Council and Complutense University (CSIC-UCM), 28040 Madrid, Spain and [4]Department of Geology, İstanbul-Cerrahpaşa University, 34850, Avcılar, İstanbul, Turkey

Abstract

This study focused on a detailed mineralogical and crystal-chemical analysis of Mg-smectites from four bentonite samples from Turkey. Mg-rich smectites, mainly associated with alkaline and evaporitic depositional conditions, are formed in environments such as salt lakes, brine springs, and sabkhas, as well as in hydrothermal systems, in some cases by transformation from other phyllosilicates. Saponite has also been documented on the surface of Mars. The systems that produce Mg-smectites are less common than those that produce dioctahedral Al-smectites and consequently Mg-rich smectites are less abundant than dioctahedral smectites. For this reason, information on nanoscale mineralogy and crystal chemistry of Mg-smectites is relatively lacking. In this study, X-ray diffraction, thermal analysis and electron microscopy were used to study Mg-smectites. The crystal chemistry of single crystals determined with analytical electron microscopy in transmission electron microscopy (AEM-TEM) revealed that all samples had notable variability in the composition of individual crystals, such that no point analysis resulted in ideal structural formulae for saponite, stevensite, sepiolite, or palygorskite. They contain SiO_2 content greater than that corresponding to a Mg-smectite, even stevensite, and often are intermediate to Mg-smectites and the sepiolite-palygorskite series. Meanwhile, the number of octahedral cations is small for fibrous clay minerals. Neither the point analysis of smectitic particles nor the mean structural formula fit properly for Mg-smectites showing crystallochemistry complexity. The results of these point analyses, in which no contamination has been observed, suggest that these smectites have intermediate compositions between trioctahedral smectites and sepiolite-palygorskite, indicating nanometer-scale intergrowths of these minerals in Mg-rich clay deposits.

Keywords: Mg-rich clay; palygorskite; saponite; stevensite; sepiolite; trioctahedral smectites

(Received: 22 May 2024; revised: 22 August 2024; accepted: 19 September 2024)

Introduction

Bentonites are frequently volcanic ash beds transformed to clayey sedimentary layers that are typically rich in dioctahedral smectites (e.g. montmorillonite). In alkaline and evaporitic depositional conditions such as salt lakes, brine springs, and sabkhas, however, bentonites tend to be rich in trioctahedral smectites that are frequently associated with the sepiolite-palygorskite minerals (Christidis and Huff, 2015; Pozo and Calvo, 2018; Andrić-Tomašević et al., 2021; Lei et al., 2022). Trioctahedral smectites, excluding hectorite and griffithite, are Mg-rich smectites. Mg-smectites can also be related to interstratified chlorite/smectite (April, 1981; Bettison-Varga and Mackinnon, 1997). Mg-smectites have also been documented in salt lakes, brine springs, and sabkhas (Singer and Galán, 1984; Chamley, 1989; Calvo et al., 2009; Galán and Singer, 2011; Pozo and Galán, 2015, among others), in salars (Bentz and Peterson, 2020), in hydrothermal deposits (Chamley, 1989; Meunier, 2005; Abd Elmola et al., 2020) and submarine chimneys (Gutiérrez-Ariza et al., 2024), and on the surface of Mars (Tirsch et al., 2018; Pascuzzo et al., 2019; Singh et al., 2021). It is also important to emphasize that Mg-smectites may form in many settings by transformation from other phyllosilicates (García-Romero and Suárez, 2022).

The genetical relationships of Mg-rich smectites with minerals from the sepiolite-palygorskite series (Suárez and García-Romero, 2013) are similar. This is because of the close stability fields of these minerals when they form by precipitation from solutions in ambient conditions (Birsoy, 2002). According to Jones (1986), a sequence exists in a typical playa lake environment, from the lake edge, where detrital minerals such as illite, kaolinite, and dioctahedral smectite are abundant, towards the center of the lake where sepiolite and Mg-rich minerals (stevensite and kerolite) are the most abundant components neoformed by direct precipitation. In between, palygorskite and saponite are dominant.

Mg-rich bentonites are relatively scarce. They appear in magnesian basins, such as the Tajo Basin in Spain (García-Romero

Corresponding author: Mercedes Suárez; Email: msuarez@usal.es
Cite this article: Lorenzo A., García-Romero E., Yeniyol M., & Suárez M. (2025). Mineralogy and crystal-chemistry of trioctahedral smectites from Turkey. *Clays and Clay Minerals* **73**, e4, 1–13. https://doi.org/10.1017/cmn.2024.35

et al., 2019; García-Rivas et al., 2018; García-Romero and Suárez, 2022; Herranz and Pozo, 2022), Amargosa Desert in the USA (Papke, 1972; Khoury et al., 1982; Miles, 2011), Santos Basin that is located offshore eastern Brazil (Carramal et al., 2022; Herlinger et al., 2023), and several areas in Anatolian Peninsula (Turkey). Turkey has numerous bentonite deposits in the Biga and Gelibolu peninsulas and in the Eskisehir-Ankara, Çankırı-Tokat, Ordu-Trabzon, Kayseri-Nevsehir-Nigde, and Malatya-Elazıg regions (İnan and Hiçsönmez, 2022). Most of them consist of dioctahedral smectites, mainly montmorillonite (Abdioğlu et al., 2004; Abdioğlu and Arslan, 2005; Arslan et al., 2010; Kadir et al., 2021, among others). However, deposits of trioctahedral smectites also exist, such as those where saponite appears together with sepiolite-palygorskite in the Neogene lacustrine sediments of the Serinhisar-Acipayam basin, Deńizli, SW Turkey (Akbulut and Kadir, 2003). Saponite also occurs with these fibrous clays in E and SW Eskişehir (Yeniyol, 2007; Yeniyol, 2012), in the Hekimhan basin (Yalçin and Bozkaya, 1995), and in the Polatli region (Karakaya and Karakaya, 2008). Additionally, stevensite has been reported in the Yenidogan area together with sepiolite (Yeniyol, 2014) and in the Bigadiç, Emet, and Kirka lacustrine basins associated with zeolites (Gündogdu et al., 1996). Furthermore, saponite has been discovered in lacustrine deposits intercalated with volcanic rocks (Das Gupta, 1996; Gündogdu et al., 1996; Abdioğlu, 2018).

The crystal-chemistry of trioctahedral smectites is not as well-known as that of dioctahedral smectites. Comparative and detailed studies have been conducted on the structural formula and layer charge of dioctahedral smectites; for example, Kaufhold (2006), Christidis and Eberl (2003), Emmerich et al. (2009), Kaufhold et al. (2017), and Christidis et al. (2023). However, few studies have focused on the crystal chemistry of trioctahedral smectites. Probably, the most-researched trioctahedral smectites are from the Tajus Basin (Spain) where industrial clays have been mined since the second half of the 20th century. There exist several studies with relevant crystal-chemical information – for example, Galán et al. (1986), Martín de Vidales et al. (1991), Pozo and Casas (1999), Cuevas et al. (1993), De Santiago et al. (1998), Cuevas et al. (2003), Steudel et al. (2017), and García-Romero et al. (2019, 2021). In these studies, smectites of the same bentonitic deposit have been classified as kerolite, kerolite-stevensite mixed-layers, stevensite, an interstratification of turbostratic talc and saponite, and as low-charge saponite. Meanwhile, García-Romero and Suárez (2022) demonstrated the mineralogical and crystal-chemical complexity of these smectites and their narrow relationship with sepiolite.

The aim of the present study was to contribute to the knowledge of the crystal-chemistry of trioctahedral smectites through a detailed study of a group of bentonites sampled from Turkey from sites with different geological origins and complex clay mineralogy.

Materials and methods

Four bentonitic samples from Turkey, labelled as C5, YA3, KT4, and YD28 were studied. YA3, YD28, and KT4 were sampled in different locations of Pliocene lacustrine sediments from the Eskisehir- Sivrihisar Basin. They derive from a dolomite-rich sedimentary Neogene sequence, where authigenetic Mg-clay minerals are abundant. The basement rocks in this area consist of metamorphic (Paleozoic blueschist) and serpentinized ultramafic rocks (Mesozoic). Neogene lacustrine sediments cover a large area stretching to the east and southeast from Eskisehir City. YD28 was sampled near the Yenidoğan village, in the upper part of the Pliocene sequence where two levels of sepiolite appear (Yeniyol, 2014). The sample corresponds to a level of dolomitic clay that appears between clayey dolomite and dolomite levels at the top of the lacustrine sequence. KT4 and YA3 samples were found close to Kepeztepe and Yörükakçayır villages (SW Eskişehir), where a sepiolite-palygorskite deposit is found (Yeniyol, 2012). KT4 corresponds to smectitic materials that occur as two separate layers (~0.1 m) at the bottom of the massive dolomites that constitutes the top of a lacustrine sequence in which dolomitic marls and dolomite beds, Pliocene in age, alternate and rest upon Upper Miocene conglomerates (Yeniyol, 2007).

C5 derives from a vein-type magnesite deposit in south Konya, where Mg-smectites were locally found with sepiolite. Mg-smectite was formed by replacement from magnesite (Yeniyol, 2020). C5 was collected at western Çayırbağı village, ~20 km from Konya City. The Mg-clay minerals were formed from pre-existing magnesite. In this area there are ophilitic complexes that consist of pyroxenite altered to serpentinite and of gabbro dykes. They were emplaced as large overthrust slabs over the older lithologies during the Upper Cretaceous and they were covered by Neogene lacustrine sediments containing clayey limestone, conglomerate, and limestone. The Çayırbağı ophiolite contains magnesite deposits formed by the interaction of CO_2-rich surface waters with serpentinite during the ophiolite emplacement. Magnesite appears as veins and stockworks in the uppermost parts. Sepiolite and Mg-smectite appear as veins intersecting each other and displaying a stockwork structure inherited from the pre-existing magnesite. These clay minerals were formed in late-stage phases under supergene conditions. Further details regarding the geology of the deposits are available in Yeniyol (1992, 2014, and 2020).

Mineralogical characterization of whole rock and <2 μm fraction was performed using X-ray diffraction (XRD). Whole-rock samples were powdered using an agate manual mortar. The <2 μm fraction was obtained after suspension in water and decantation and studied as oriented aggregates under ambient conditions, after solvation with ethylene glycol and heating at 550°C. A Bruker D-8 advance XRD diffractometer using CuKα radiation and a graphite monochromator was employed, with a step size of 0.05°2θ and counting time of 1 s per step. The quantification of the crystalline phase was performed using the Full Pattern Summation method (Butler and Hillier, 2021a), implemented with the powdR package (Butler and Hillier, 2021b) in RStudio. Prior to the analysis, the samples were prepared using the spray drying procedure (Hillier, 1999). Whitney and Evans (2010) was followed for abbreviations of minerals.

Chemical analyses of major and trace elements were performed on the bulk samples using inductively coupled plasma-atomic emission spectrometry (ICP-AES) (with aqua regia digestion) and inductively coupled plasma-mass spectrometry (ICP-MS) by ACTLABS laboratories in Canada. The 4Lithoresh package was used. Information on the analytical procedures and detection limits for each element is available at: http://www.actlabs.com.

Thermal analysis and Fourier-transform infrared (FT-IR) spectroscopy were performed at the Unidad de Técnicas Geológicas, at the Universidad Complutense (Madrid). The FT-IR spectrometer used was a Nicolet Nexus that works in the middle IR between 400 and 4000 cm^{-1} on KBr pellets. Thermal analysis consisted of simultaneous differential thermal analysis (DTA), thermogravimetric analysis (TGA), and differential scanning calorimetry (DSC). They were obtained with a TA Instrument

SDT-Q600, which enables working from room temperature (~25°C) to 1300°C with a heating rate of 10°C min^{-1} in an atmosphere of synthetic air.

The transmission electron microscopy (TEM) study was performed optimizing the experimental conditions to avoid structural modifications using a low beam intensity (<500 counts on the CCD camera). The chemical composition of the samples was obtained using analytical electron microscopy (AEM) with TEM, both in natural and homoionized with Ca^{2+} samples, to ascertain the structural formula of smectites and the interlaminar cations (García-Romero et al., 2021). For the homoionization of the smectites, powdered samples were immersed in a 1 M $CaCl_2$ solution at room temperature for three successive 24 h baths. Thereafter, the chloride solutions were removed until the chloride was completely removed, washing the samples with successive distilled water and centrifugation baths. The absence of chloride was confirmed with dilute $AgNO_3$. Homoionized samples were labelled as C5-Ca, YA3-Ca, KT4-Ca, and YD28-Ca. The samples for TEM were prepared by depositing a drop of diluted clay suspension onto copper grids with a holey carbon film. The analyses were conducted at the Centro de Instrumentación Científica (CIC), University of Granada, Spain, with a HAADF Thermo Fisher Scientific TALOS F200X microscope. Structural formulas were calculated for 2:1 phyllosilicates – that is, for $O_{20}(OH)_4$. All Fe present in the samples was considered as Fe^{3+} (owing to the limitation of the technique); however, the possible existence of scarce Fe^{2+} cannot be excluded.

The scanning electron microscopy (SEM) for samples labelled as C5 was performed using the FEI Quanta FEG 450 SEM apparatus at the Istanbul University–Cerrahpaşa, Department of Chemical Engineering. The sample analyses of YD28, KT4, and YA3 were conducted at the Scientific and Technological Research Council of Türkiye, Marmara Research Center (TÜBİTAK-MAM) using a Jeol JSM-6335F field emission SEM equipped with an Oxford Inca energy dispersive spectrometer (EDS). For analyses, gold-coated chips were used.

Results and Discussion

X-ray diffraction

XRD patterns of raw powdered samples showed high purity of smectites. C5 was the purest sample, with 89% smectite and a small amount of palygorskite as impurity. Dolomite was the major non-clay mineral identified in three of the studied samples, except for C5, in which this carbonate was absent (Fig. 1; Table 1). The sample YA3 had the smallest smectite content (≈43%). The purest sample was C5; its XRD pattern showed the characteristic asymmetric and broad bands corresponding to the hk0 reflections of smectites together with a broad basal 001 reflection. This sample presented a shoulder in the broad 001 reflection located at 8.26°2θ (10.69 Å) that could correspond to 110 of palygorskite. KT4 and YA3 were similar; both had dolomite impurities, which were more abundant in the YA3 sample (15% and 19%, respectively). In both samples, there was a minor reflection of palygorskite – more intense and better defined in the YA3 sample, minor quantities of quartz (26.6°2θ, 3.34 Å), and a small peak at 12.11°2θ (7.30 Å) corresponding to serpentine. Additionally, quartz, feldspar, chlorite, and illite were identified. These minerals represent the detrital components, whereas smectite and palygorskite were neoformed (Yeniyol, 2012). Finally, YD28 presented only minor quantities of dolomite. It stood out with the broad band at small angles, between 4.08°2θ and 8.03°2θ, indicating the small number of layers per coherent scattering domain (CSD) in the smectite (Yeniyol, 2014; Yeniyol, 2020).

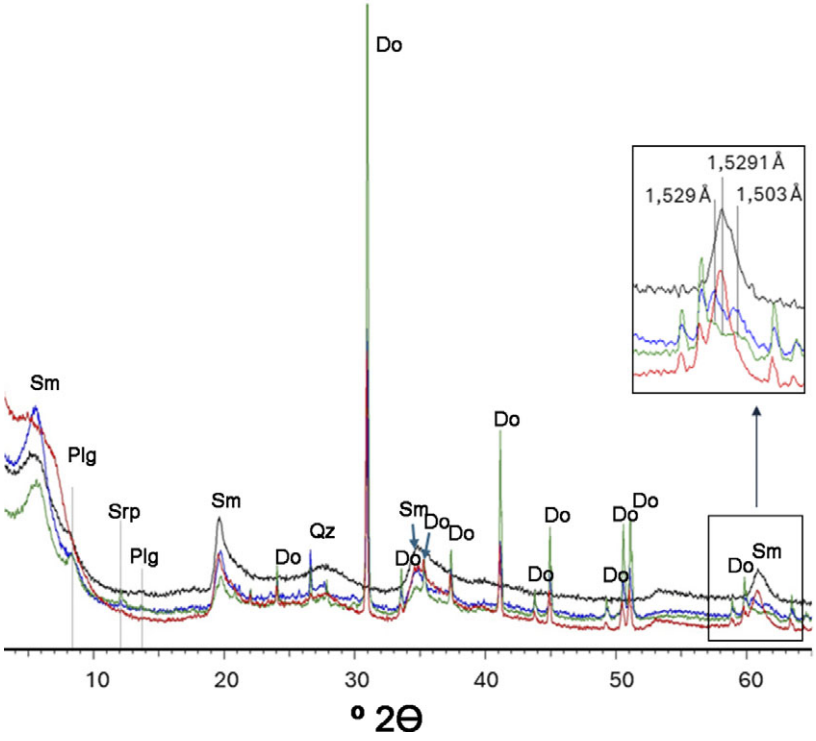

Figure 1. X-ray diffraction patterns of raw samples. Black: C5; blue: KT4; green: YA3; and red: YD28. Sm = smectite, Plg = palygorskite, Qz = quartz, Do = dolomite, Srp = serpentine. Detailed area (inset) contains the smectite 060 *d*-spacings.

Table 1. Mineralogical composition (in percentages) from XRD

	Sme	Plg	Qz	Dol	Ilt	K-Fsp	Srp	Dol (Ch. A.)
C5	89	10	1					
KT4	64	7	2	19	5	3	Trace	22
YA3	43	9	1	44	3		Trace	46
YD28	85			15				16

Sme = smectite, Plg = palygorskite, Qz = quartz, Dol = dolomite, Ilt = illite, K-Fsp = potassic felspar, Srp = serpentine; Dol (Ch. A.) is the content in dolomite calculated from the content in CaO of the chemical analysis.

Oriented aggregates and their treatments (Fig. 2) confirmed smectite as the majority component and the presence of minor amounts of palygorskite in the KT4 and YA3 samples and illite, together with scarce chlorite. Palygorskite in the KT4 and YA3 samples had a 110 reflection at 10.6 Å, which corresponds to a Mg-rich palygorskite (Statopoulou et al., 2011). This implied that they had some sepiolite polysomes (Suárez and García-Romero, 2011).

The Biscaye index of smectites (Biscaye, 1965) ranges between –0.2 (YD28) and 0.4 (KT4). This implies the presence of smectites with low crystallinity, especially in the YD28 sample, in which, as previously indicated, there was no ordering in the [001] direction, even though the hk0 reflection was explicit (Fig. 1). In that sample, a wide band appeared from 12 Å in oriented aggregates that moved toward smaller angles (~17 Å) in EG as corresponding to smectites. These XRD patterns of YD28 appeared like Pink Clays from Tajo (García-Romero et al., 2021; García-Romero and Suárez, 2022), where saponite appeared as tiny crystals with few 2:1 stacked layers.

The 060 reflection appeared mainly at approximately 1.52 Å in all samples, which implies that all smectites were trioctahedral. Minor differences were observed in this reflection (Fig. 1). C5 and YD28 were explicitly trioctahedral, whereas YA3 and KT4 showed a more dioctahedral component, as could be deduced from the double peak. The *d*-spacing was not so low as 1.49 Å; however, two maxima were present at 1.528 Å and 1.503 Å (Fig. 1). The major dioctahedral component in the YA3 and KT4 samples was palygorskite, and a minor proportion of illite was also present as revealed by the oriented aggregate patterns. These two samples had chlorite as traces as revealed by the small peak at approximately 14 Å after heating at 550°C and serpentine appearing at 7.28 Å. The presence of the 110 reflection of the palygorskite was visible in the C5 and KT4 raw samples as a shoulder and as a peak in EG patterns, while it appeared as a peak in the YA3 sample.

The mineralogical assemblages found in these samples, formed by trioctahedral smectite with carbonates and sepiolite-palygorskite, are common (Christidis and Huff, 2015). The neoformation of dolomite and saponite in lacustrine environments, similar to the formation environments of YA3, KT4, and YD28 (Yeniyol, 2012; Yeniyol, 2014), is frequently encountered in the Mediterranean area. Most of them are considered as Miocene or Pliocene in terms of age (Kadir et al., 2002; Akbulut and Kadir, 2003; Karakaya and Karakaya, 2008); however, Holocene sediments with this mineralogical composition have also been identified (Abdelwahab et al., 2022). The studied samples correspond to a Mg-rich clay paragenesis in which saponite is a major mineral together with fibrous minerals of the sepiolite-palygorskite polysomatic series. In the sample with the greatest palygorskite content, the values for ^{IV}Al and octahedral vacancies, calculated from the d_{002} spacing and the equations proposed by Suárez et al. (2007) were 0.95 per half unit cell (p.h.u.c.) and 0.65 p.h.u.c., respectively. These corresponded to Mg-palygorskite, which contained a large percentage of sepiolite polysomes (Suárez and García-Romero, 2011; Suárez and García-Romero, 2013).

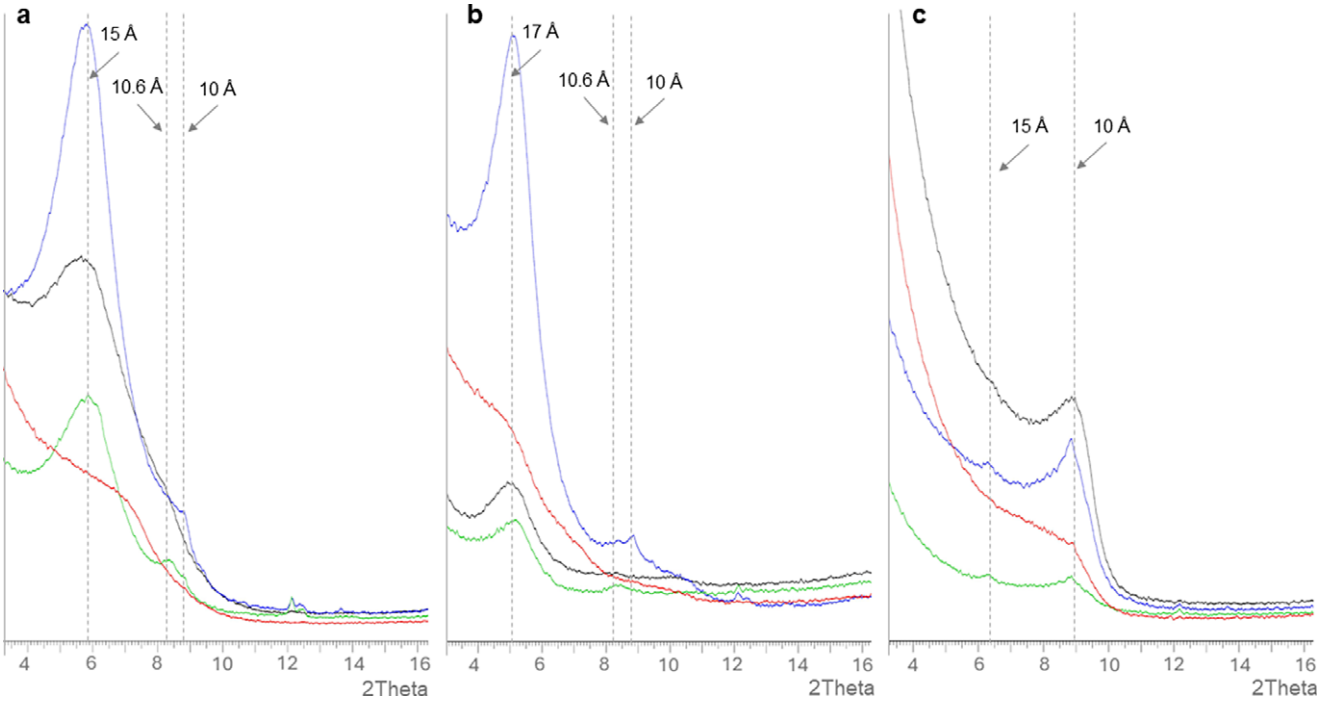

Figure 2. X-ray diffraction patterns of the oriented aggregates of the <2 μm fraction. Black: C5; blue: KT4; green: YA3; and red: YD28. (a) Normal environment, (b) ethylene glycol, and (c) heated at 550°C for 2 h.

Chemical analysis

The chemical composition was in accordance with the mineralogical content (Tables 1 and 2), as the logical and most abundant elements included Si, Mg, and Ca, ranging in the case of SiO_2 between 27.6 and 50.65%, MgO between 16.68 and 23.52%, and CaO between 0.34 and 4.68%. The loss on ignition value ranged between 20.16% (C5) and 28.2% (YA3), and its variation was related to both clay minerals and dolomite content (except C5, which does not contain dolomite). The C5 sample was the richest in Fe, being Fe^{3+}-majority in comparison with other samples, because FeO was under 1%, even under the limit of detection in the YA3 sample. The sample with a smaller amount of Al_2O_3 was YD28. The contents of minor and trace elements are presented in Table 3. C5 and YD28 showed smaller values than that in KT4 and YA3, with notable exceptions. Cr had concentrations >200 ppm, except in sample YD28, which was also depleted in Co and Ni. Sample C5 stood out for its small values of Sr and Cs on the one hand and a significantly greater value of Ni on the other. Sample KT4 had the greatest concentration of elements belonging to the REE group, followed by sample YA3. The abundance of As is notable, except in sample C5 with <5 ppm, as it appears trioctahedral smectites tend to contain greater quantities of As than dioctahedral smectites (Lorenzo et al., 2024).

VNIR-SWIR spectroscopy

The reflectance spectra of the samples were similar (Fig. 3), without appreciable bands in the visible wavenumber range with two large absorption bands in the NIR region; the first at approximately 1400 nm and the second at 1900 nm, both corresponding to smectites. This is because of the overtones of fundamental stretching vibrations and combinations of stretching and bending modes of the structural OH^- groups bonded to octahedral cations and H_2O present in both the interlayer of smectites and adsorbed

Table 2. Content of major elements in percentage of oxides

Sample	SiO_2	Al_2O_3	TiO_2	Fe_2O_3	FeO	MnO	MgO	CaO	Na_2O	K_2O	P_2O_5	LOI
C5	50.65	4.07	0.109	5.22	0.80	0.054	17.65	0.34	0.02	0.39	<0.01	20.16
KT4	37.64	6.96	0.301	3.16	0.30	0.050	16.68	6.70	0.12	1.37	0.04	25.50
YA3	27.60	4.83	0.234	3.02	<0.1	0.052	19.06	14.1	0.07	0.71	0.03	28.20
YD28	42.35	1.40	0.077	0.03	0.50	0.01	23.52	4.86	0.04	0.23	0.03	25.44

LOI = loss on ignition.

Table 3. Content of minor and trace elements in ppm

Sample	V	Cr	Co	Ni	Cu	Zn	Ga	Ge	As	Rb	Sr
C5	17	200	36	1620	<10	<30	5	0,7	<5	34	40
KT4	53	290	16	280	10	40	9	0,8	11	101	238
YA3	43	260	12	350	20	90	6	0,7	13	53	385
YD28	33	<20	1	<20	<10	<30	2	<0.5	16	25	366
	Y	Zr	Nb	Mo	Ag	In	Sn	Sb	Cs	Ba	La
C5	1.2	73	5.5	<2	<0.5	<0.1	1	<0.2	2.2	40	5.12
KT4	12.2	92	9.4	<2	<0.5	<0.1	2	0.6	71.2	115	20.80
YA3	8.2	57	7.9	<2	<0.5	<0.1	1	0.4	41.4	64	12.00
YD28	2.2	25	2.4	<2	<0.5	<0.1	<1	0.3	42.5	59	5.20
	Ce	Pr	Nd	Sm	Eu	Gd	Tb	Dy	Ho	Er	Tm
C5	13.40	0.88	2.83	0.40	0.06	0.29	0.04	0.22	0.05	0.14	0.022
KT4	36.20	4.18	14.90	3.00	0.44	2.19	0.36	2.19	0.41	1.31	0.183
YA3	19.60	2.50	8.86	1.70	0.32	1.55	0.26	1.37	0.26	0.80	0.118
YD28	9.34	1.05	3.42	0.57	0.13	0.47	0.08	0.44	0.08	0.22	0.027
	Yb	Lu	Hf	Ta	W	Tl	Pb	Bi	Th	U	
C5	0.14	0.019	1.8	0.48	0.6	0.09	<5	<0.1	3.86	0.39	
KT4	1.24	0.185	2.1	0.82	4.0	0.40	16	0.2	10.90	1.16	
YA3	0.84	0.134	1.2	1.24	1.5	0.17	15	0.1	5.84	0.86	
YD28	0.17	0.026	0.6	0.37	<0.5	<0.05	<5	<0.1	1.87	4.88	

Data with < symbol indicate that the element was under the detection limit.

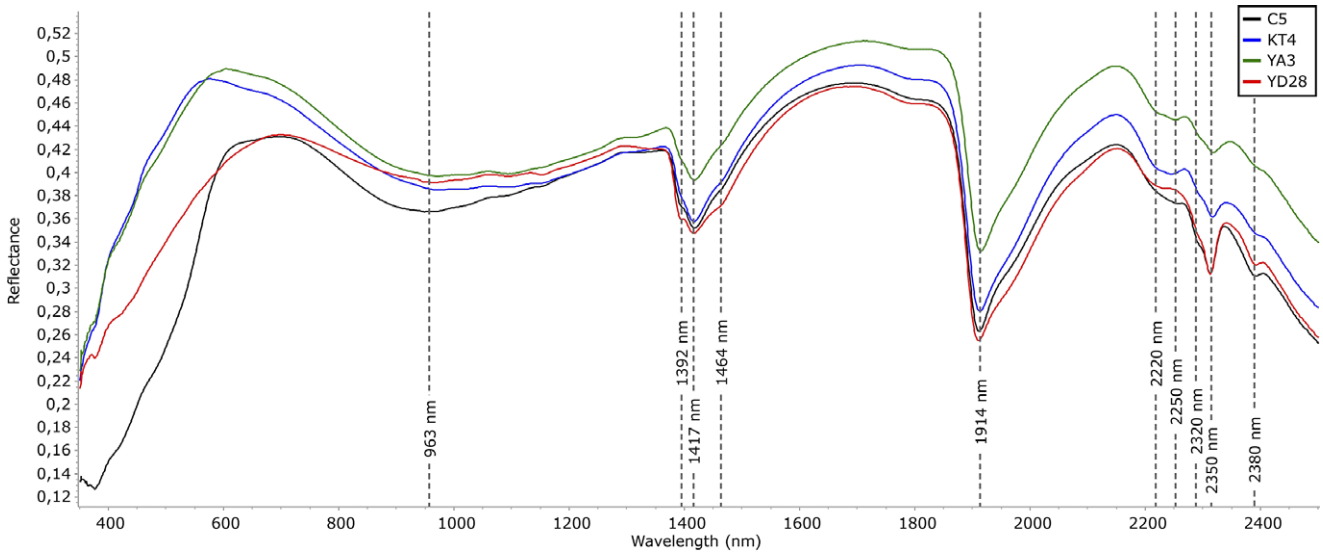

Figure 3. VNIR-SWIR spectra of the studied samples.

on the surface (Bishop et al., 2002; Madejová et al., 2017). Smaller bands owing to M-OH^{-} vibrations appeared between 2200 and 2400 nm, which depend on the octahedral content. Therefore, the spectra were explicitly marked by the smectites and the major absorption features corresponding to dolomite could not be observed. In dolomite, the characteristic absorption features of carbonates were due to vibrational modes of the CO_3^{2-} anion with a diagnostic absorption feature in the approximately 2300 nm region and a reflectance decline from 2400 nm (Cloutis et al., 2010; Gaffey, 1986). Additionally, dolomite had small absorption features at approximately 1860, 1980, and 2140 nm. The diagnostic band at 2300 nm could be overlapped with that of trioctahedral smectite; however, the reflectance decline at larger wavenumber was the same in the samples with dolomite (KT4, YA3, and YD28) as in C5, which did not have dolomite. This implies that dolomite impurities did not affect the interpretation of the smectite signal in the spectra. This agrees with Santamaría et al. (2024), who suggested that kaolinite–dolomite mixtures should contain at least 65% dolomite to enable the identification of its characteristic spectral features.

In fact, owing to the mineralogical similarities, the spectra of C5 and YD28 constituted one couple whereas KT4 and YA3 constituted another. An extremely wide absorption was observed in the visible region at approximately 536 nm for sample C5; this could be related to the presence of minor quantities of hematite or Fe^{3+} as octahedral cation (Báscones et al., 2020). Focusing on the region between 1000 and 2500 nm, two areas of special interest were present in these samples. First, the band at approximately 1400 nm owing to OH^{-} vibrations appeared in all samples with two shoulders (Fig. 3), which is the characteristic of trioctahedral smectites and sepiolite. The shoulder at 1390 nm became a peak in the YD28 sample (Fig. 3), which is characteristic of trioctahedral smectites. In the samples with greater impurity content (YA3 and KT4), this effect manifested itself as a shoulder. Another conspicuous region was 2200 to 2400 nm, where various bands (in position and/or intensity) or shoulders were identified – all related to the stretching and bending combinations involving various octahedral cations in clay minerals (Madejová et al., 2017). The absorptions (Fig. 3) located at approximately 2350 and 2388 nm were related to trioctahedral 3Mg-OH bonds. Minor effects at 2220 and 2250 nm were due to the presence of octahedral Al and Fe^{3+} cations. These were more intense in YA3 and KT4, whereas those at 2350 and 2388 nm were more intense in C5 and YD28. This is in good agreement with the mineralogy of these two samples, because YA3 and KT4 have more palygorskite and illite in the clay fraction, whereas C5 and YD28 are richer in Mg-smectite.

Thermal analysis

Thermogravimetric analysis (TGA), differential thermal analysis (DTA), and differential scanning calorimetry (DSC) were also conducted (see Figs S1–S3 in the Supplementary material). The derivative of the TGA curves (DTG) was obtained for each sample (Fig. 4). Thermogravimetric curves showed progressive loss of weight, although with notable differences among the samples. These losses were related to the peaks in DTG and the endothermic effects in DTA and DSC curves, with only an exothermic effect at high temperature (approximately 810°C). Trioctahedral smectites constitute the major component in the samples together with dolomite. Smectites had only three signals in the range of temperature studied: (1) at low temperature, dehydration of adsorbed and interlayer water occurred, which implies endothermic effect and a loss of weight; (2) dehydroxylation occurred at >700°C, and is related to an endothermic effect and loss of weight; and (3) the transformation into an anhydrous phase at >800°C, which was shown as an exothermic effect. Scarce references are available on the thermal behavior of trioctahedral smectites that differ from dioctahedral smectites, in which *cis* and *trans* vacants affect the dehydroxylation temperature (Drits et al., 1998). Dehydroxylation of the octahedral sheet of trioctahedral smectites occurred just before phase transformation at highest temperatures, usually at >700°C. These smectites had no other endothermic or exothermic effect in the region between 100 and 700°C owing to the lack of octahedral vacancies (Steudel et al., 2017; Derkowski and Kuligiewicz, 2023).

Conversely, the major impurity present in three samples was dolomite, which had a characteristic endothermic peak due to: (1) thermal decomposition into calcite + MgO (periclase) and (2) the thermal decomposition of calcite at temperatures that depends on CO_2 pressure. The first effect appears as a shoulder

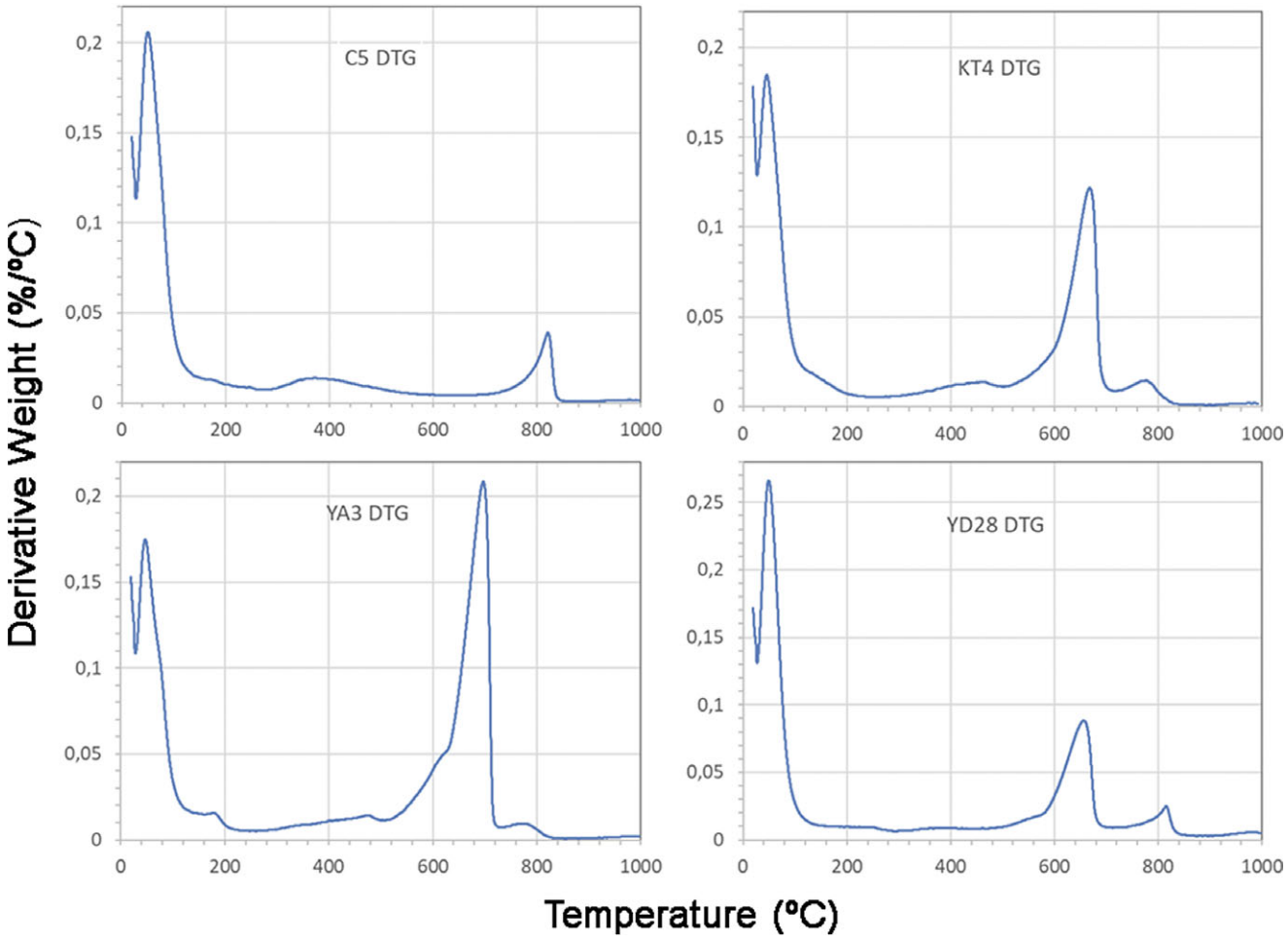

Figure 4. DTG of the studied samples.

or change of inflexion of the second endothermic peak in the DTG curve (Resio, 2023). According to Li and Messing (1983), the notable variability in decomposition temperatures of dolomite and differences may be due to experimental factors, such as sample size, grain size, heating rate, atmospheric conditions, and the influence of other minerals, which can affect dolomite decomposition extensively. In the studied samples, the endothermic peak related to dolomite, with an associated loss of weight, is approximately 700°C in the three samples containing dolomite. Dolomite can show an effect under 700°C when ground for several hours (Ozao et al., 1991). However, the samples studied here were ground within a few minutes. The low temperature for dolomite decomposition is probably related to the influence of clay minerals. The intensity of the major peak (between 650 and 700°C) in the DTG in the three samples with dolomite was in accordance with the proportion of dolomite calculated via both XRD and chemical analysis (Tables 1 and 2). A large correlation was observed between the calculated quantity of dolomite and the intensity of the peak at 700°C in the DTG curve (see Fig. S4 in the Supplementary material). The more intense effect was observed in sample YA3 = 46% dolomite, followed by KT4 = 22% dolomite, and YD28 = 16% dolomite.

In the samples studied, the major effect at the lowest temperature was an endothermic peak at <100°C due to the dehydration of adsorbed and interlayer water, with a loss of weight between 9.77% (YA3) and 12.44% (YD28). This was in good agreement with the content in smectite because these samples contain 43% and 85% smectite, respectively. C5 and YA3 showed a small shoulder in the DTG and ADT at approximately 80°C (Fig. 4; Fig. S1), probably because of the presence of different interlayer cations in the smectite (El-Barawy et al., 1986). The YA3 sample and KT4 and C5 with extremely small intensity, also showed a peak or shoulder at approximately 175°C in DTG (Fig. 3), which corresponded to palygorskite dehydration because of the release of zeolitic water in the fibrous mineral (Frost and Ding, 2003). The presence of Mg-palygorskite, identified via XRD, also influenced the region between 200 and 500°C because this mineral has a wide endothermic effect due to the partial dehydration and folding of the structure between 350 and 450°C (Frost and Ding, 2003).

At the highest temperatures, dehydroxylation and phase transformation of smectite occurred, as previously mentioned, and a small exothermic peak appeared in the DTA and DSC curves with the loss of weight in the TGA (Figs S1 and S3; Fig. 3), although the loss of weight is smaller than expected according to the mineralogical content of the samples, which could indicate a progressive dehydroxylation of the samples from lower temperatures. On the other hand, the exothermic effect due to the recrystallization of a new phase was present in all samples with small differences in the temperature. In KT4 and YA3, recrystallization appeared at 778°C whereas C5 and YD28 made another couple

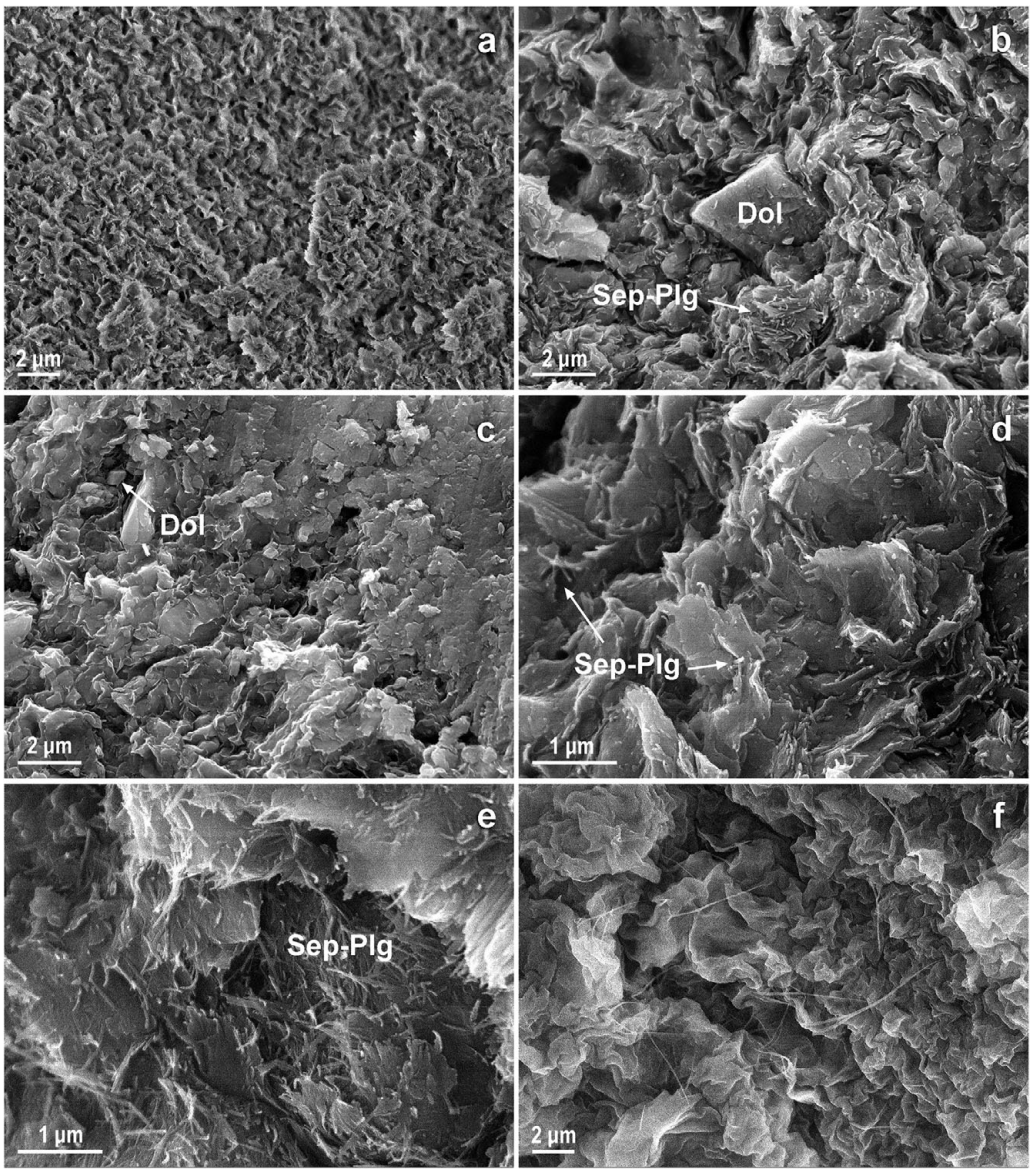

Figure 5. Representative images of the samples by SEM. (a) C5; (b) KT4; (c,d,e) YA3; (f) YD28. Dol = dolomite, Plg = palygorskite, Sep = sepiolite.

displaying recrystallization effect at 823°C. DTG curves also displayed structural similarities between KT4 and YA3 on the one hand, and between C5 and YD28 on the other hand (Fig. 4). According to Vogels et al. (2005), after an initial amorphization, pyroxene- and olivine-like structures could form. The temperature difference required for the phase transformation in these samples could be related to crystal-chemical differences, size of crystals, or the influence of other minerals. According to Drits et al. (1998), the more heterogeneous the octahedral composition, the wider the range of smectite dehydroxylation temperature. In this case, the range in dehydroxylation temperatures indicated that the samples are not completely trioctahedral.

Scanning electron microscopy

The samples were studied via scanning electron microscopy (SEM) to observe their microstructure. C5 appeared a highly homogeneous material (Fig. 5a), with un-oriented small aggregates of laminar particles with pores of a few hundred nanometers. The samples KT4 and YA3 were mutually similar (Fig. 5b–e). The aggregates of laminar particles in these two samples showed a closer microstructure than in C5, and they surrounded dispersed dolomite crystals that occasionally attained the size of several microns (Fig. 5b). The YD28 sample was completely different, appearing like corrugated textile, where it was impossible to differentiate particles with the level of magnification used (Fig. 5f). This sample showed an open texture like that of the sepiolite shown by García-Romero and Suárez (2013), which were obtained after suspension in water and sedimentation of samples.

Furthermore, in C5, KT4, and YA3, isolated fibrous particles or tiny bundles were observed occasionally (Fig. 5b,d,e). However, a unique characteristic of these three samples was the presence of laminar particles that presented fibrous terminations at their edges. The fibers were well developed only in a few cases (Fig. 5e). In all cases, sepiolite-palygorskite fibers were not well developed, lacking the typical bundles that characterize these minerals. However, they appeared intimately related to smectites, exhibiting a narrow

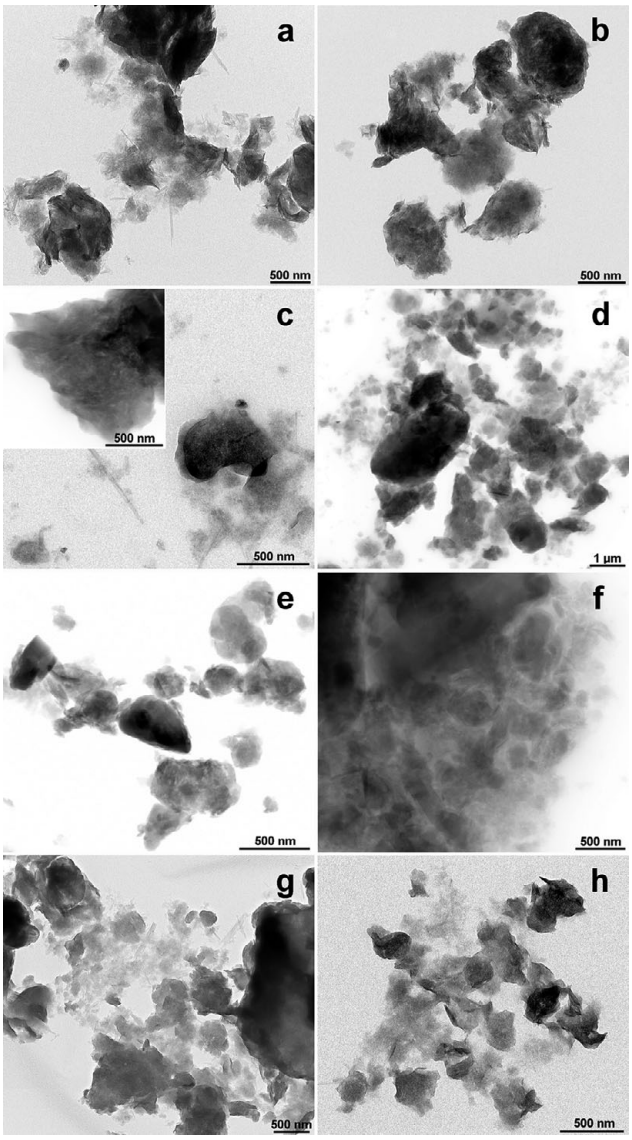

Figure 6. Representative images of smectites under TEM. (a) C5, (b) C5-Ca, (c) KT4, (d) KT4Ca, (e) YA3, (f) YA3-Ca, (g) YD28, and (h) YD28-Ca.

textural relationship, which suggested transformation reactions involving smectite and the fibrous mineral.

Transmission electron microscopy and point analyses

The morphology of single crystals of smectites was studied via TEM (Fig. 6). According to mineralogical characterization, the characteristic laminar morphology with *diffuse* edges were the most abundant in the samples. However, some fibrous crystals were also observed in all samples. The size of smectite crystals rarely exceeded 0.5 µm in their large dimension. KT4 and YA3 also showed scarce surrounded laminar particles of illite, 1–2 µm in size. This mineral was also identified via XRD in these samples.

The samples were analyzed under natural conditions after homoionization with Ca^{2+} to ascertain octahedral Mg^{2+} and interlayer contents (García-Romero et al., 2019). No isolated fibers or mixed particles were analyzed. The major element contents in oxides of all smectitic particles analyzed before and after homoionization (Tables S1 and S2 in the Supplementary material) showed large variability. All data were fitted as 2:1 phyllosilicates, for $O_{20}(OH)_4$ (Table S3 in the Supplementary material). The mean structural formulae were obtained from the mean and standard deviation of the oxide contents and the structural formula fitted from the mean values of major elements contents for both natural and homoionized samples (Table 4).

The content of CaO increased in the homoionic samples, confirming the successful exchange of cations. The differences among the samples before and after homoionization indicated that Mg was an interlayer cation in the natural samples, as expected. Therefore, the Ca-samples were suitable for studying the crystal-chemistry of these smectites. The contents in SiO_2, Al_2O_3, Fe_2O_3, and MgO were plotted both for natural and Ca-homoionized smectites (Fig. 7). Greater modification occurred for the YA3 sample after homoionization. The proportion of mean values of these oxides varied in all samples after homoionization. SiO_2 increased in all samples, except for C5, whereas the other oxides decreased, mainly MgO, logically. This indicates that Mg^{2+} was an interlayer cation in natural samples. The samples differed: C5 had the smallest SiO_2 and greatest Fe_2O_3 content, whereas YD28 had the greatest SiO_2 and MgO contents. KT4 and YA3 had the smallest MgO and greatest Al_2O_3 content among these samples. A certain proportion of K^+ remained after homoionization, mainly in sample KT4 – and to a lesser extent, in YA3 and C5 (Fig. 7; Table S2). This K^+ must be related to a minor proportion of interstratified mica-type layers in the smectite crystals (Hoang-Minh et al., 2019; García-Romero et al., 2021) – even in C5, in which mica had not been identified via XRD.

The Fe_2O_3 content calculated via AEM was greater in C5, intermediate in KT4 and YA3, and smaller in YD28. This agreed with the depth of the wide absorption feature found at approximately 900 nm in the VNIR-SWIR spectra and with the background in the XRD-patterns that was greater with higher Fe content in the samples owing to the fluorescence of this element.

Considering the Ca-homoionized samples only, the mean formulae obtained of individual point analyses did not fit properly for trioctahedral smectites, except for the C5-Ca sample. In this sample, both the mean formula and all particles analyzed fitted as a low-charge saponite (between –0.40 and –0.54 of layer charge per unit cell), with octahedral Al^{3+} and Fe^{3+}, which led to an octahedral occupancy between 5.25 and 5.50 octahedral cations per unit cell (p.u.c.) (Table S4). Additionally, this sample showed the smallest standard deviation values for all structural parameters calculated. However, the point analysis of KT4, YA3, and YD28 did not fit properly as smectite. In the group of formulae obtained for smectites of the KT4 and YA3 samples (Table S4), most particles did not fit as smectites. This is because both the number of silicon atoms, the layer charge, and the number of occupied octahedral positions were not compatible with trioctahedral smectites, nor with any other 2:1 phyllosilicate.

In YA3-Ca, only 27.6% of the particles fitted as saponite. The other particles did not fit as 2:1 minerals because they had >8 Si atoms p.u.c. In fact, the number of tetrahedral positions reached 8.57 p.u.c. This occurred for the YD28 sample; however, in this case, all formulae contained >8 Si atoms p.u.c., with a mean value of 8.25 and a standard deviation of 0.08 (Table S4). After Ca-homoionization, both the values obtained for layer and interlayer charges increased and the number of octahedral cations decreased with respect to the values calculated in the non-homoionic samples (Tables S3 and S4), in accordance with García-Romero et al. (2021). According to the number of octahedral cations, smectites in the C5-Ca and YD28-Ca samples were explicitly trioctahedral, in good agreement with the 060 reflection in XRD at 1.52 Å. However,

Table 4. Major elements (% weight of oxides) from point analyses by AEM, mean values, and standard deviation (*SD*), and structural formula fitted for $O_{22}(OH)_4$ from these mean values

	C5	*SD*	C5Ca	*SD*	KT4	*SD*	KT4Ca	*SD*	YA3	*SD*	YA3Ca	*SD*	YD28	*SD*	YD28Ca	*SD*
% SiO_2	63.01	±0.75	62.67	±0.36	64.32	±1.90	66.77	±1.65	56.85	±2.01	65.80	±2.89	66.29	±1.23	68.89	±0.77
% Al_2O_3	5.41	±0.59	5.55	±0.29	9.93	±1.31	8.02	±1.25	11.58	±3.05	6.31	±0.94	2.30	±1.32	1.87	±0.72
% Fe_2O_3	6.56	±1.01	6.60	±0.66	4.10	±0.38	3.33	±0.39	5.57	±0.67	4.05	±1.00	0.94	±0.57	0.57	±0.23
% MgO	24.18	±0.81	23.14	±0.87	18.61	±1.77	17.83	±2.00	22.25	±3.98	16.09	±1.12	28.98	±2.34	26.76	±0.60
% CaO	0.46	±0.05	1.64	±0.10	1.57	±0.88	2.98	±1.06	2.28	±1.41	7.16	±2.21	1.04	±0.50	1.69	±0.16
% K_2O	0.38	±0.07	0.40	±0.06	1.49	±0.54	1.07	±0.31	1.47	±0.85	0.59	±0.14	0.45	±0.60	0.23	±0.13
Si	7.71		7.7		7.81		8.07		7.07		8.07		8		8.26	
Al(IV)	0.29		0.3		0.19		0		0.93		0		0		0	
ΣIV	8		8		8		8.07		8		8.07		8		8.26	
Al	0.49		0.5		1.23		1.14		0.76		0.91		0.33		0.26	
Fe^{3+}	0.6		0.61		0.37		0.3		0.52		0.37		0.09		0.05	
Mg	4.41		4.24		3.37		3.21		4.12		2.94		5.21		4.78	
ΣVI	5.5		5.35		4.97		4.65		5.41		4.22		5.62		5.09	
Ca	0.06		0.22		0.2		0.39		0.3		0.94		0.13		0.22	
K	0.03		0.06		0.23		0.17		0.23		0.09		0.07		0.03	
QIV	–0.29		–0.3		–0.19		0.28		–0.93		0.28		0		1.04	
QVI	0.11		–0.19		–0.45		–1.26		0.09		–2.05		–0.34		–1.51	
QL	–0.18		–0.49		–0.64		–0.98		–0.84		–1.97		–0.34		–0.47	
QIL	0.18		0.49		0.64		0.94		0.84		1.97		0.34		0.47	

ΣIV = number of tetrahedral cations, ΣVI = number of octahedral cations, QIV = tetrahedral charge, QVI = octahedral charge, QL = layer charge, QIL = interlayer charge.

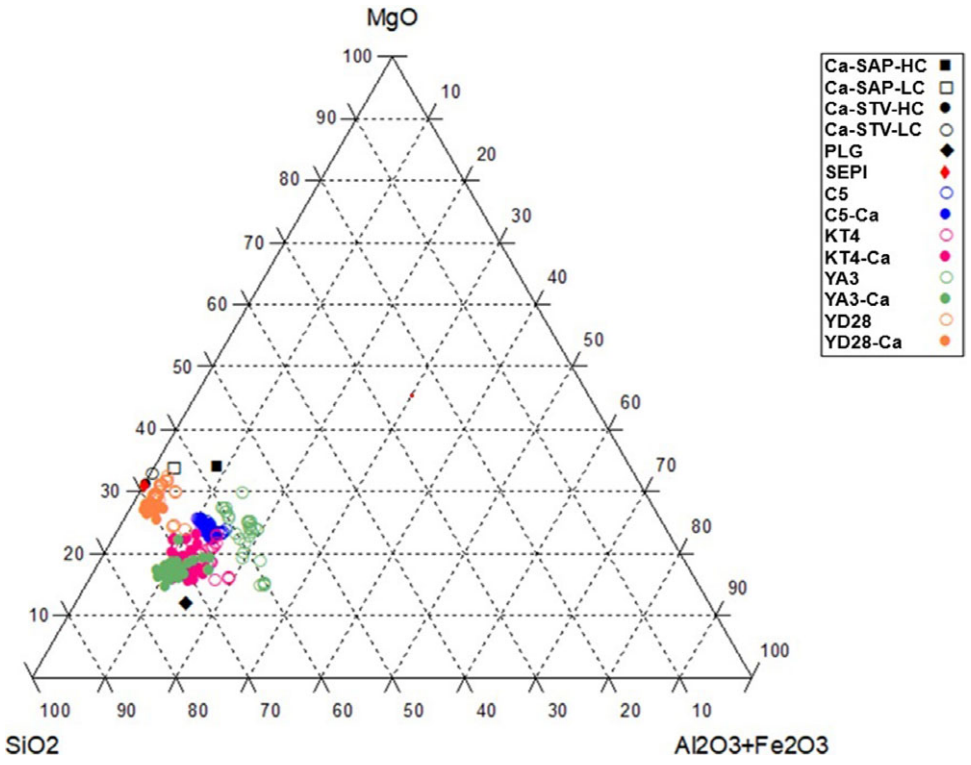

Figure 7. Chemical data of point analyses for both natural and Ca-homoionic samples. Key: Ca-SAP-HC = Ca-high charge saponite, Ca-SAP-LC = Ca-low charge saponite, Ca-STV-HC = Ca-high charge stevensite, Ca-STV-LC = Ca-low charge stevensite, PLG = palygorskite, SEPI = sepiolite.

the mean formulae fitted for KT4-Ca and YA3-Ca had dioctahedral properties because the numbers of octahedral cations were 4.65 and 4.22, respectively. These values are anomalous because, although they presented a double peak at 1.50–1.52 Å, the second was more intense, and therefore, the smectites – the majority phyllosilicates in those samples – must have been trioctahedral. However, the number of octahedral cations was not the only parameter that failed to fit properly in the mean structural formulae of KT4-Ca and YA3-Ca. These two samples and Y28-Ca had >8 Si atoms (p.u.c.). These structural formulae were obtained via point analysis. Contamination with other mineral particles could not be claimed to explain these anomalous compositions. This is because it occurred for all analyses in the YD28 sample and for most of them in KT4-Ca and YA3-Ca. Additionally, analysis locations were chosen on surfaces of smectitic particles.

Crystal-chemistry of clay minerals is complex. Clay crystals may contain minor quantities of substances adsorbed on their surfaces and frequently appear as interstratified with other clay minerals in such a manner that they are often structurally heterogeneous. The excess of Si could be related to the presence of amorphous silica adsorbed on the surface of the smectitic particles (Moore and Reynolds, 1997) or the presence of intergrowth of other minerals with a larger ratio of Si/octahedral cations, such as sepiolite-palygorskite.

To visualize the variability of the composition of the smectitic particles, the results of the point analyses were plotted in two ternary plots together with the composition of ideal sepiolite, palygorskite, and saponite and stevensite of low and high charges (Fig. 7). This plot showed large variability of composition in natural and homoionic samples. The composition of these particles must lie in the region between palygorskite and most magnesian clays (sepiolite, stevensite, and low-charge saponite). Both the mean structural formula and all point analyses of KT4 and YA3 plotted between palygorskite and the region richest in Mg minerals, C5 plotted between high-charge saponite and palygorskite, and YD28 plotted closer to the sepiolite and stevensite. These projections show that the smectitic particles have intermediate composition between laminar and fibrous minerals, although only laminar particles were analyzed.

Final remarks

These samples can be described as bentonites, because their major minerals were trioctahedral smectites, with impurities of dolomite and minor quantities of minerals of the sepiolite-palygorskite series.

The most interesting features were related to the crystal-chemistry of the smectitic particles. All point analyses of smectites in these samples did not fit properly for Mg-smectites, having a composition intermediate between smectites and sepiolite-palygorskite. According to the XRD and the observations under TEM, all samples had a proportion of fibers intimately mixed with the small laminar particles. In a few cases, contamination may have occurred because of the mixture of particles in the analysis. However, the crystal-chemistry of these smectitic particles is complex and the results of the point analysis cannot be explained solely by the possible contamination of fibers. Conversely, it must be related to the structural complexity of these smectites in which intergrowths/interstratification could exist.

This study will contribute to the knowledge of the crystal-chemistry of Mg-smectites. It shows narrow relationships among Mg-smectites and sepiolite-palygorskite. However, more studies on the crystal-chemistry and structure of Mg-clays are needed in order to improve the knowledge of these relationships among Mg-clay minerals.

Supplementary material. The supplementary material for this article can be found at http://doi.org/10.1017/cmn.2024.35.

Data availability statement. The datasets generated during and/or analysed during the current study are available from the corresponding author on reasonable request.

Author contributions. Mercedes Suárez and Adrian Lorenzo: conceptualization. Mercedes Suárez and Emilia García-Romero: funding acquisition. All authors contributed to the acquisition, analysis, and interpretation of data. All authors contributed to writing, review and editing original draft.

Financial support. Funded by Grant PID-2019-106504RB funded by MCIN/ AEI/ 10.130 39/501100011033.

Competing interests. The authors declare none.

References

Abd Elmola, A., Asaad, A., Patrier, P., Beaufort, D., Ballini, M., & Descostes, M. (2020). Clay mineral signatures of fault-related fluid flows in a sandstone reservoir: a case study from the Teloua Formation, Tim Mersoï Basin, Niger. *Journal of African Earth Sciences*, *168*, art. no. 103840. doi: 10.1016/j.jafrearsci.2020.103840

Abdelwahab, S., Hassan, H.B., & El-Sabagh, M.E.I. (2022). Geochemistry and mineralogy of Qaroun Lake and relevant drain sediments, El-Fayoum. *Egypt Journal of African Earth Sciences*, *185*, art. no. 104388. doi: 10.1016/j.jafrearsci.2021.104388

Abdioğlu, E. (2018). Alteration mineralogy, mineral chemistry and stable isotope geochemistry of the Eocene pillow lavas from the Trabzon area, NE Turkey. *Journal of African Earth Sciences*, *138*, 149–166. doi: 10.1016/j.jafrearsci.2017.11.014

Abdioğlu, E., & Arslan, M. (2005). Mineralogy, geochemistry and genesis of bentonites of the Ordu area, NE Turkey. *Clay Minerals*, *40*, 131–151. doi: 10.1180/0009855054010161.

Abdioğlu, E., Arslan, M., Kolayli, H., & Kadir, S. (2004). Mineralogical and geochemical characteristics of the Tirebolu (Giresun) bentonite deposits, NE Turkey. *Geochimica et Cosmochimica Acta*, Goldschmidt Conference, p. A416.

Akbulut, A., & Kadir, S. (2003). The geology and origin of sepiolite, palygorskite and saponite in Neogene lacustrine sediments of the Serinhisar-Acipayam basin, Deñizli, SW Turkey. *Clays and Clay Minerals*, *51*, 279–292. doi: 10.1346/CCMN.2003.0510304

Andrić-Tomašević, N., Simić, V., Mandic, O., Životić, D., Suárez, M., & García-Romero, E. (2021). An arid phase in the Internal Dinarides during the early to middle Miocene: Inferences from Mg-clays in the Pranjani Basin (Serbia). *Palaeogeography, Palaeoclimatology, Palaeoecology*, *562*, art. no. 110145. doi: 10.1016/j.palaeo.2020.110145

April, R.H. (1981). Trioctahedral smectite and interstratified chlorite/smectite in Jurassic strata of the Connecticut Valley. *Clays and Clay Minerals*, *29*, 31–39. doi: 10.1346/CCMN.1981.0290105

Arslan, M., Abdioğlu, E., & Kadir, S. (2010). Mineralogy, geochemistry, and origin of bentonite in upper Cretaceous pyroclastic units of the Tïrebolu area, Gïresun, Northeast Turkey. *Clays and Clay Minerals*, *58*, 120–141. doi: 10.1346/CCMN.2010.0580112

Báscones, A., Suárez, M., Ferrer-Juliá, M., García-Meléndez, E., Colmenero-Hidalgo, E., & Quirós, A. (2020). Characterization of clay minerals and Fe oxides through diffuse reflectance spectroscopy (VNIR-SWIR. *Revista de Teledetección*, *2020*, 49–57. doi: 10.4995/raet.2020.13331

Bentz, J.L., & Peterson, R.C. (2020). The formation of clay minerals in the mudflats of Bolivian salars. *Clays and Clay Minerals*, *68*, 115–134. doi: 10.1007/s42860-020-00065-x

Bettison-Varga, L, & Mackinnon, I.D.R. (1997). The role of randomly mixed-layered chlorite/smectite in the transformation of smectite to chlorite. *Clays and Clay Minerals*, *45*, 506–516. doi: 10.1346/CCMN.1997.0450403

Birsoy, R. (2002). Formation of sepiolite-palygorskite and related minerals from solution. *Clays and Clays Minerals*, *50*, 736–745.

Biscaye, P.E. (1965). Mineralogy and sedimentation of recent deep-sea clay in the Atlantic Ocean and adjacent seas and oceans. *Bulletin of the Geological Society of America*, *76*, 803–832. doi: 10.1130/0016-7606

Bishop, J., Madejová, J., Komadel, P., & Fröschl, H. (2002). The influence of structural Fe, Al and Mg on the infrared OH bands in spectra of dioctahedral smectites. *Clay Minerals*, *37*, 607–616. https://doi.org/10.1180/0009855023740063.

Butler, B.M., & Hillier, S. (2021a). Automated full-pattern summation of X-ray powder diffraction data for high-throughput quantification of clay-bearing mixtures. *Clays and Clay Minerals*, *69*, 38–51. https://doi.org/10.1007/s42860-020-00105-6

Butler, B.M., & Hillier, S. (2021b). powdR: an R package for quantitative mineralogy using full pattern summation of X-ray powder diffraction data. *Computers and Geosciences*, *147*. https://doi.org/10.1016/j.cageo.2020.104662

Calvo, J.P., Blanc-Valleron, M.M., Rodríguez-Arandía, J.P., Rouchy, J.M., & Sanz, M.E. (2009). Authigenic clay minerals in continental evaporitic environments. In Thiry, M., & Simon-Coinçon, R. (eds), *Palaeoweathering, Palaeosurfaces and Related Continental Deposits*, pp. 129–151. Blackwell Publishing Ltd, Oxford, UK. https://doi.org/10.1002/9781444304190.ch5

Carramal, N.G., Oliveira, D.M., Cacela, A.S.M., Cuglieri, M.A.A., Rocha, N.P., Viana, S.M., Toledo, S.L.V., Pedrinha, S., & De Ros, L.F. (2022). Paleoenvironmental insights from the deposition and diagenesis of Aptian Pre-salt magnesium silicates from the Lula field, Santos basin, Brazil. *Journal of Sedimentary Research*, *92*, 12–31. doi: 10.2110/jsr.2020.139

Chamley, H. (1989). *Clay Sedimentology*, 1st edn. Springer, Berlin, Heidelberg. https://doi.org/10.1007/978-3-642-85916-8

Christidis, G.E., & Eberl, D.D. (2003). Determination of layer-charge characteristics of smectites. *Clays and Clay Minerals*, *51*, 644–655.

Christidis, G.E., Chryssikos, G.D., Derkowski, A., Dohrmann, R., Eberl, D.D., Joussein, E., & Kaufhold, S. (2023). Methods for determination of the layer charge of smectites: a critical assessment of existing approaches. *Clays and Clay Minerals*, *71*, 25 – 53.

Christidis, G., & Huff, W. (2015). Geological aspects and genesis of bentonites. *Elements*, *5*, 93–98. doi: 10.2113/gselements.5.2.93

Cloutis, E.A., Grasby, S.E., Last, W.M., Léveillé, R., Osinski, G.R., & Sherriff, B.L. (2010). Spectral reflectance properties of carbonates from terrestrial analogue environments: Implications for Mars. *Planetary and Space Science*, *58*, 522–537. https://doi.org/10.1016/j.pss.2009.09.002

Cuevas, J., Pelayo, M., Rivas, P., & Leguey, S. (1993). Characterization of Mg-clays from the Neogene of the Madrid Basin and their potential as backfilling and sealing material in high level radioactive waste disposal. *Applied Clay Science*, *7*, 383–406.

Cuevas, J., Vigil de La Villa, R., Ramírez, S., Petit, S., Meunier, A., & Leguey, S. (2003). Chemistry of Mg smectites in lacustrine sediments from the Vicálvaro sepiolite deposit, Madrid Neogene basin (Spain). *Clays and Clay Minerals*, *5*, 457–472.

Das Gupta, S. (1996). Bentonite deposits intercalated with the Rajmahal volcanic rocks of eastern India. *Journal of Southeast Asian Earth Sciences*, *13*, 133–137. doi: 10.1016/0743-9547(96)00014-1

Derkowski, A., & Kuligiewicz, A. (2023). Thermal analysis and thermal reactions of smectites: a review of methodology, mechanisms, and kinetics. *Clays and Clay Minerals*, *70*, 946–972. doi: 10.1007/s42860-023-00222-y

De Santiago, C., Suárez, M., GarciaRomero, E., Domínguez Díaz, M.C., & Doval, M. (1998). Electron microscopic study of the illie-smectite transformation in the bentonites from Cerro del Águila (Toledo, Spain). *Clay Minerals*, *33*, 501–510.

Drits, V.A., Lindgreen, H., Salyn, A.L., Ylagan, R., & McCarty, D.K. (1998). Semiquantitative determination of trans-vacant and cis-vacant 2:1 layers in illites and illite-smectites by thermal analysis and X-ray diffraction. *American Mineralogist*, *83*, 1188–1198.

El-Barawy, K.A., Girgis, B.S., & Felix, N.S. (1986). Thermal treatment of some pure smectites. *Thermochimica Acta*, *98*, 181–189.

Emmerich, K., Wolters, F., Kahr, G., & Lagaly, G. (2009). Clay profiling: the classification of montmorillonites. *Clays and Clay Minerals*, *57*, 104–114.

Frost, R.L., & Ding, Z. (2003). Controlled rate thermal analysis and differential scanning calorimetry of sepiolites and palygorskites. *Thermochimica Acta*, *397*, 119–128. doi: 10.1016/S0040-6031(02)00228-9

Gaffey, S.J. (1986). Spectral reflectance of carbonate minerals in the visible and near infrared (0.35–2.55 microns): calcite, aragonite, and dolomite. *American Mineralogist*, *71*, 151–162. https://doi.org/10.1029/JB092iB02p01429

Galán, E., Álvarez, A., & Esteban, M.A. (1986). Characterization and technical properties of a Mg-rich bentonite. *Applied Clay Science*, *1*, 295–309.

Galán, E., & Singer, A. (2011). *Developments in Clay Science* (1st edn), 270 pp. Elsevier B.V, Amsterdam.

García-Rivas, J., Suárez, M., Torres, T., Sánchez-Palencia, Y., García-Romero, E., & Ortiz, J.E. (2018). Geochemistry and biomarker analysis of the bentonites from Esquivias (Toledo, Spain). *Minerals*, *8*, 291. https://doi.org/10.3390/min8070291

García-Romero, E., Lorenzo, A., García-Vicente, A., Morales, J., García Rivas, J., & Suárez, M. (2021). On the structural formula of smectites: a review and new data on the influence of exchangeable cations. *Journal of Applied Crystallography*, *54*, 251–262. doi: 10.1107/S1600576720016040

García-Romero, E., Manchado, E.M., Suárez, M., & García Rivas, J. (2019). Spanish bentonites: a review and new data on their geology, mineralogy, and crystal chemistry. *Minerals*, *9*, 696.

García-Romero, E., & Suárez, M. (2013). Sepiolite–palygorskite: textural study and genetic considerations. *Applied Clay Science*, *86*, 129–144. https://doi.org/10.1016/j.clay.2013.09.013

García-Romero, E., & Suárez, M. (2022). HRTEM evidence of Tajo Basin mineralogical complexity: crystal chemistry and genetic relationship. *Applied Clay Science*, *224*, 1–13. https://doi.org/10.1016/j.clay.2022.106515

Gündogdu, M.N., Yalçin, H., Temel, A., & Clauer, N. (1996). Geological, mineralogical and geochemical characteristics of zeolite deposits associated with borates in the Bigadiç, Emet and Kirka Neogene lacustrine basins, western Turkey. *Mineralium Deposita*, *31*, 492–513. doi: 10.1007/BF00196130

Gutiérrez-Ariza, C., Barge, L.M., Ding, Y., Cardoso, S.S.S., McGlynn, S.E., Nakamura, R., Giovanelli, D., Price, R., Lee, H.E., Huertas, F.J., Sainz-Díaz, C.I., & Cartwright, J.H.E. (2024). Magnesium silicate chimneys at th9e Strytan hydrothermal field, Iceland, as analogues for prebiotic chemistry at alkaline submarine hydrothermal vents on the early Earth. *Progress in Earth and Planetary Science*. https://doi.org/10.1186/s40645-023-00603-w

Herlinger, R., Jr, De Ros, L.F., Surmas, R., & Vidal, A. (2023). Residual oil saturation investigation in Barra Velha Formation reservoirs from the Santos Basin, Offshore Brazil: a sedimentological approach. *Sedimentary Geology*, *448*, art. no. 106372. doi: 10.1016/j.sedgeo.2023.106372

Herranz, J.E., & Pozo, M. (2022). Sepiolite and other authigenic Mg-clay minerals formation in different Palustrine environments (Madrid Basin, Spain). *Minerals*, *12*, 987. doi: 10.3390/min12080987

Hillier, S. (1999). Use of an air brush to spray dry samples for X-ray powder diffraction. *Clay Minerals*, *34*, 127–135.

Hoang-Minh, T., Kasbohm, J., Nguyen-Thanh, L., Nga, P.T., Lai, L.T., Duong, N. T., Thanh, N.D., Thuyet, N.T.M., Anh, D.D., Pusch, R., Knutsson, S., & Ferreiro-Mahlmann, R. (2019). Use of TEM-EDX for structural formula identification of clay minerals: a case study of Di Linh bentonite, Vietnam. *Journal of Apply Crystallography*, *52*, 133–147. https://doi.org/10.1107/S1600576718018162

İnan, S., & Hiçsönmez, Ü. (2022). Adsorption studies of radionuclides by Turkish minerals: a review. *Journal of the Turkish Chemical Society, Section A: Chemistry*, *9*, 579–600. doi: 10.18596/jotcsa.1074651

Jones, B.F. (1986). Clay mineral diagenesis in lacustrine sediments. *U.S. Geological Survey Bulletin*, *1578*, 291–300.

Kadir, S., Baş, H., & Karakaş, Z. (2002). Origin of sepiolite and loughlinite in a neogene volcano-sedimentary lacustrine environment, Mihaliççik-Eskişehir, Turkey. *Canadian Mineralogist*, *40*, 1091–1102. doi: 10.2113/gscanmin.40.4.1091

Kadir, S., Külah, T., Erkoyun, H., Uyanık, N.Ö., Eren, M., & Elliott, W.C. (2021). Mineralogy, geochemistry, and genesis of bentonites in Upper Cretaceous pyroclastics of the Bereketli member of the Reşadiye Formation, Reşadiye (Tokat), Turkey. *Applied Clay Science*, *204*, 106024. doi: 10.1016/j.clay.2021.106024

Karakaya, M.C., & Karakaya, N. (2008). Mineralogic and geochemical features of Neogene aged sedimentary units of Polatli, sw Ankara (Turkey). *8th International Scientific Conference on Modern Management of Mine Producing, Geology and Environmental Protection, SGEM 2008*, *1*, 139–147.

Kaufhold, S. (2006). Comparison of methods for the determination of the layer charge density (LCD) of montmorillonites. *Applied Clay Science*, *34*, 14–21.

Kaufhold, S., Kremleva, A., Krüger, S., Rösch, N., Emmerich, K., & Dohrmann, R. (2017). Crystal-chemical composition of dicoctahedral smectites: an energy-based assessment of empirical relations. *ACS Earth and Space Chemistry*, *1*, 629–636. doi: 10.1021/acsearthspacechem.7b00082

Khoury, H.N., Eberl, D.D., & Jones, B.F. (1982). Origin of magnesium clays from the Amargosa Desert, Nevada. *Clays and Clay Minerals*, *30*, 327–336. doi: 10.1346/CCMN.1982.0300502

Li, M.Q., & Messing, G.L. (1983). Chloride salt effects on the decomposition of dolomite. *Thermochimica Acta*, *68*, 1–8. doi: 10.1016/0040-6031(83)80373-6

Lei, H., Huang, W., Jiang, Q., & Luo, P. (2022). Genesis of clay minerals and its insight for the formation of limestone marl alterations in Middle Permian of the Sichuan Basin. *Journal of Petroleum Science and Engineering*, *218*, 111014. doi: 10.1016/j.petrol.2022.111014

Lorenzo, A., Sánchez-Santos, J.M., Rivas, M.J., García-Romero, E., Suárez, M. (2024) Geochemistry of bentonites: A statistical analysis of trace element distribution in smectites. *Applied Clay Science*, *257*, doi: 10.1016/j.clay.2024.107449.

Madejová, J., Gates, W.P., & Petit, S. (2017). IR spectra of clay minerals. *Developments in Clay Science*, *8*. https://doi.org/10.1016/B978-0-08-100355-8.00005-9

Martín de Vidales, J.L., Pozo, M., Alia, J.M., García Navarro, F., & Rull, R. (1991). Kerolite-stevensite mixed-layers from the Madrid Basin, Central Spain. *Clay Minerals*, *26*, 329–342.

Meunier, A. (2005). *Clays*. Springer-Verlag, Berlin/Heidelberg. doi: 10.1007/b138672

Miles, W.J. (2011). Amargosa sepiolite and saponite: geology, mineralogy, and markets. *Developments in Clay Science*, *3*, 265–277. doi: 10.1016/B978-0-444-53607-5.00011-6

Moore D.M., & Reynolds R.C. (1997). *X-Ray Diffraction and the Identification and Analysis of Clay Minerals*, 378 pp. Oxford University Press, Oxford, New York.

Ozao, R., Ochiai, M., Yamazaki, A., & Otsuka, R. (1991). Thermal analysis of ground dolomites. *Thermochimica Acta*, *183*, 183–198. doi: 10.1016/0040-6031(91)80458-U

Pascuzzo, A.C., Mustard, J.F., Kremer, C.H., & Ebinger, E. (2019). The formation of irregular polygonal ridge networks, Nili Fossae, Mars: implications for extensive subsurface channelized fluid flow in the Noachian. *Icarus*, *319*, 852–868. doi: 10.1016/j.icarus.2018.10.020

Papke, K.G. (1972). A sepiolite-rich playa deposit in southern Nevada. *Clays and Clay Minerals*, *20*, 211–215. doi: 10.1346/CCMN.1972.0200405

Pozo, M., & Casas, J. (1999). Origin of kerolite and associated Mg clays in palustrine-lacustrine environments. The Esquivias deposit (Neogene Madrid Basin, Spain). *Clay Minerals*, *34*, 395–418.

Pozo, M., & Calvo, J.P. (2018). An overview of authigenic magnesian clays. *Minerals*, *8*, 520. doi: 10.3390/min8110520

Pozo, M., & Galán, E. (2015). Magnesian clay deposits: mineralogy and origin. In M. Pozo, & E. Galán (eds), *Magnesian Clays: Characterization, Origin and Applications*, pp. 175–227. AIPEA Educational Series, *2*, Digilabs, Bari, Italy.

Resio, L.C. (2023). Dolomite thermal behaviour: a proposal to establish a definitive decomposition mechanism in a convective air atmosphere. *Open Ceramics*, *15*, 100405. doi: 10.1016/j.oceram.2023.100405

Santamaría-López, Á., Suárez, M., & García-Romero, E. (2024). Detection limits of kaolinites and some common minerals in binary mixtures by short-wave infrared spectroscopy. *Applied Clay Science*, *250*, 107269. doi: 10.1016/j.clay.2024.107269

Singh, D., Singh, P., Roy, N., & Mukherjee, S. (2021). Investigation of mineral assemblages in a newly identified endorheic playa near Huygens basin on Mars and their astrobiological implications. *Icarus*, *372*, 114757. doi: 10.1016/j.icarus.2021.114757

Singer, A., & Galán, E. (1984). *Developments in Sedimentology*. Elsevier Science Publishers, B.V., Amsterdam.

Statopoulou, E.T., Suárez, M., García-Romero, E., Sánchez del Río, M., Kacandes, G.H., Gionis, V., & Chryssikos, G.D. (2011). Trioctahedral entities in palygorskite: near-infrared evidence for sepiolite-palygorskite polysomatism. *European Journal of Mineralogy*, *23*, 567–576.

Steudel, A., Friedrich, F., Schuhmann, R., Ruf, F., Sohling, U., & Emmerich, K. (2017). Characterization of a fine-grained interstratification of turbostratic talc and saponite. *Minerals*, *7*, 5. doi: 10.3390/min7010005

Suárez, M., & García-Romero, E. (2011). Advances in the crystal chemistry of sepiolite and palygorskite. *Developments in Clay Science*, *3*, 33–65. doi: 10.1016/B978-0-444-53607-5.00002-5

Suárez, M., & García-Romero, E. (2013). Sepiolite-palygorskite: a continuous polysomatic series. *Clays and Clay Minerals*, *61*, 461–472.

Suárez, M., García-Romero, E., Sánchez del Río, M., Martinetto, P., & Dooryhée, E. (2007). The effect of the octahedral cations on the dimensions of the palygorskite cell. *Clay Minerals*, *42*, 287–297.

Tirsch, D., Bishop, J.L., Voigt, J.R.C., Tornabene, L.L., Erkeling, G., & Jaumann, R. (2018). Geology of central Libya Montes, Mars: aqueous alteration history from mineralogical and morphological mapping. *Icarus*, *314*, 12–34. doi: 10.1016/j.icarus.2018.05.006

Vogels, R.J.M.J., Kloprogge, J.T., Geus, J.W., & Beers, A.W.F. (2005). Synthesis and characterization of saponite clays: Part 2. *Thermal stability*. American Mineralogist, *90*, 945–953.

Whitney, D.L., & Evans, B.W. (2010). Abbreviations for names of rock forming minerals. *American Mineralogist*, *95*, 185–187. doi: 10.2138/am.2010.3371

Yalçin, H., & Bozkaya, Ö. (1995). Sepiolite-palygorskite from the Hekimhan region (Turkey). *Clays and Clay Minerals*, *43*, 705–717. doi: 10.1346/CCMN.1995.0430607

Yeniyol, M. (1992). Geology, mineralogy and genesis of the Yenidoğan (Sivrihisar). sepiolite deposit. *Mineral Research and Exploration Bulletin of Turkey*, *114*, 71–84.

Yeniyol, M. (2007). Characterization of a Mg-rich and low-charge saponite from the Neogene lacustrine basin of Eskişehir, Turkey. *Clay Minerals*, *42*, 541–548. doi: 10.1180/claymin.2007.042.4.10

Yeniyol, M. (2012). Geology and mineralogy of a sepiolite-palygorskite occurrence from SW Eskişehir (Turkey). *Clay Minerals*, *47*, 93–104. doi: 10.1180/claymin.2012.047.1.93

Yeniyol, M. (2014). Characterization of two forms of sepiolite and related Mg-rich clay minerals from Yenidog an (Sivrihisar, Turkey). *Clay Minerals*, *49*, 91–108. doi: 10.1180/claymin.2014.049.1.08

Yeniyol, M. (2020). Transformation of magnesite to sepiolite and stevensite: characteristics and genesis (Çayirbaği, Konya, Turkey) *Clays and Clay Minerals*, *68*, 347–360. doi: 10.1007/s42860-020-00083-9